International Symposium
On Turbulence and Shear Flow
Phenomena (TSFP-9)
June 30 - July 3, 2015 *Melbourne, Australia*

TURBULENT CHEMICAL AND THERMONUCLEAR FLAMES: INTRINSIC INSTABILITY AND ANISOTROPIC TURBULENCE AMPLIFICATION

Alexei Y. Poludnenko, Brian D. Taylor
Naval Research Laboratory
Washington, D.C. 20375 U.S.A.
alexei.poludnenko@nrl.navy.mil

ABSTRACT

In our previous study (Poludnenko, 2015), we presented the analysis of the intrinsic stability of high-speed turbulent reacting flows. A systematic survey of a wide range of turbulent intensities and system sizes showed that turbulent flames in the regimes considered are intrinsically unstable even in the absence of the surrounding combustor walls or obstacles, which can support the thermoacoustic feedback. In particular, three effects were observed. 1) The turbulent flame speed, S_T, can develop pulsations with the observed peak-to-peak amplitude $S_T^{max}/S_T^{min} > 10$. 2) Unstable burning results in the periodic pressure build-up and the formation of pressure waves or shocks, when S_T approaches or exceeds the speed of a Chapman-Jouguet deflagration. 3) Coupling of pressure gradients formed during pulsations with density gradients across the flame leads to the anisotropic amplification of turbulence inside the flame volume and flame acceleration.

In this work we extend prior analysis, which relied on a simplified single-step reaction model, by demonstrating existence of the pulsating flame instability in two realistic reactive systems: chemical flames in atmospheric H_2-air mixtures and thermonuclear flames in degenerate, relativistic plasmas found in stellar interiors. Finally, we also consider the dependence of the instability on the system size by performing a direct numerical simulation containing 32 billion cells in a domain twice larger than considered by Poludnenko (2015). No significant change in the instability dynamics is observed, though further analysis of this question for different Karlovitz and Damköhler numbers is required.

INTRODUCTION

Hydrodynamic flows containing exothermic reaction fronts, or flames, exhibit a rich variety of unstable phenomena. Detailed understanding of such instabilities is of significant practical importance since, ultimately, they critically control the dynamics of burning in the host system. Of particular interest here are intrinsic flame instabilities, which are independent of the external factors such as the overall geometry of the combustor, since such instabilities are generally much more difficult to control in a practical setting. In this context, historically, the primary focus of both theoretical and experimental studies has been on various hydrodynamic (e.g., Landau-Darrieus), thermodiffusive (e.g., cellular), and body-force (e.g., Rayleigh-Taylor) instabilities of premixed laminar flames (Williams, 1985).

Realistic combustion systems, such as an aircraft jet engine, however, generally rely on turbulent flames for their operation. The question of turbulent flame stability has been primarily considered in the context of burning in confined environments with walls or obstacles. In such situations, thermoacoustic instabilities result from the resonant coupling between the exothermic process and the acoustic field, which it generates in the interior of a combustor (Poinsot & Veynante, 2005; Kadowaki & Hasegawa, 2005; Candel *et al.*, 2013). A critical aspect here is that such instabilities, which are intimately tied to the host system, can potentially be efficiently suppressed, or even completely eliminated, e.g., by changing the combustor geometry.

At the same time, prior direct numerical simulations (DNS) of turbulent premixed flames suggest that such flames can exhibit significant variations in their key dynamical characteristics, in particular flame structure and burning speed, even in the absence of the surrounding combustor walls and under the most idealized circumstances of a statistically steady, homogeneous, isotropic upstream turbulence. For instance, DNS by Nishiki *et al.* (2002) and Bell *et al.* (2006) modeled flame interaction in an unconfined domain with a relatively low intensity turbulence with Damköhler number $Da \approx 17-18$ in Nishiki *et al.* (2002) and $Da \approx 1.5$ in Bell *et al.* (2006), and with Karlovitz number $Ka \sim 1$ in both cases. The maximum peak-to-peak amplitude of the turbulent burning velocity $S_T^{max}/S_T^{min} \lesssim 2.0$ was observed. In contrast, in our earlier work (Poludnenko & Oran, 2010, 2011), we considered a much higher intensity turbulence with the integral velocity $U_l = 18.5 S_L$ and scale $l = 1.9\delta_L$, where S_L and δ_L are, respectively, the speed and the thermal width of a laminar flame (cf. case 6 in Fig. 1). Even though U_l in the upstream flow varied only by a few percent over the course of the calculation, resulting turbulent flame speed exhibited significant variability with $S_T^{max}/S_T^{min} \approx 3$.

Recently, we carried out a systematic investigation of the intrinsic stability of premixed turbulent flames in the thin reaction zones regime (Poludnenko (2015), hereafter P15). In particular, that study surveyed a wide range of turbulent conditions, which are marked as cases $14-18$ in the classical combustion regime diagram (Fig. 1).

The key result of that study was the demonstration that turbulent flames can indeed exhibit significant variability of S_T. This is illustrated for cases S18 and S16 (P15) in Figs. 2a and 3a (also see Table 1). For instance in S16, S_T was observed to vary by more than an order of magnitude in the course of the simulation. The primary source of

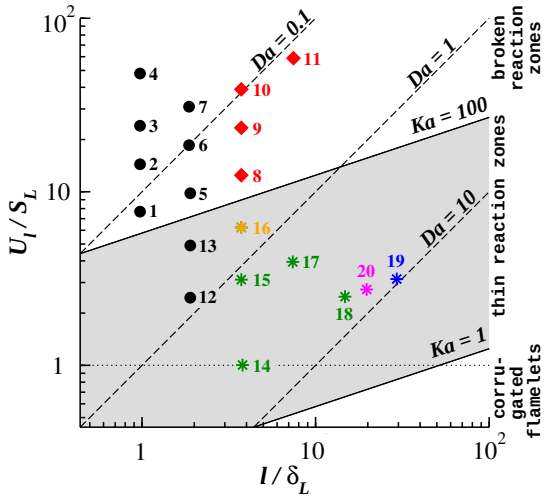

Figure 1. Summary of the combustion regimes modeled in the NRL Turbulent Premixed Flame Database. Regimes 16, 19, and 20 are discussed here, while other cases were presented in earlier papers, namely case 6 in Poludnenko & Oran (2010, 2011), cases $1-11$ in Poludnenko *et al.* (2011), cases $5-7$ and 12, 13 in Hamlington *et al.* (2011, 2012), and cases $14-18$ in Poludnenko (2015). Red diamonds mark cases, in which turbulent flames were previously found to exhibit spontaneous DDT (Poludnenko *et al.*, 2011), while stars mark pulsatingly unstable regimes.

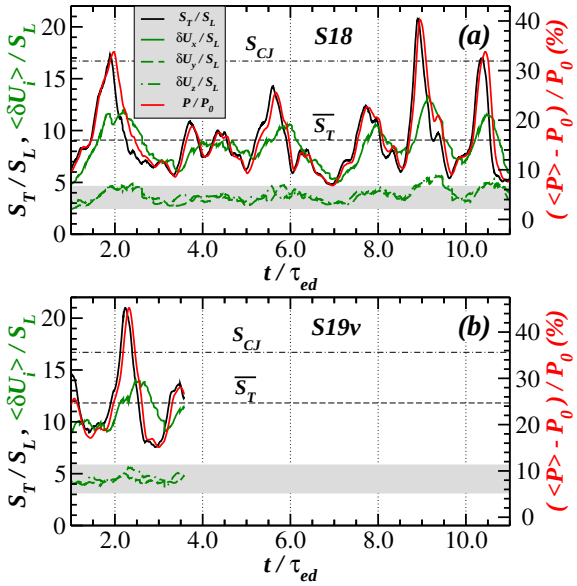

Figure 2. Evolution of the key dynamical characteristics of the flame in simulations S18 (Poludnenko, 2015) and S19v. Shown are the normalized turbulent flame speed, S_T, (black line, left axis), turbulent velocity fluctuations, $\langle \delta U_i \rangle$, (green lines, left axis), and the relative variation (in percent) of the cold fuel pressure, $\langle P \rangle$, (red line, right axis). $\langle \delta U_i \rangle$ and $\langle P \rangle$ are averages over the flame-brush volume, and P_0 is the initial fuel pressure in the domain. Horizontal lines show the time-averaged turbulent flame speed, $\overline{S_T}$ (dashed), and the CJ deflagration speed, S_{CJ} (dash-dot). The lower and upper boundaries of the shaded gray regions mark, respectively, turbulent integral and r.m.s. velocities in the cold upstream flow, U_l and U_{rms}. Note that the horizontal and left vertical axes in both panels have the same scale to facilitate comparison between the two cases.

such instability is the resonant state between the continuous creation of the flame surface by turbulence and its intermittent rapid destruction by flame collisions. This process is illustrated in Fig. 4, which shows the change in the flame structure in the course of a typical pulsation. As shown in P15, with increase in turbulent intensity $U_l > S_L$, flame surface consumption through flame self-propagation becomes progressively less important. As a result, in the absence of flame collisions (Fig. 4a), the flame surface grows exponentially under the action of turbulence, as it would for a passively advected interface. Such flame folding makes the flame surface more convolved and greatly increases the overall burning rate. At the same time, it also results in the eventual formation of extended regions of flame collision (Fig. 4b), which rapidly consume the flame surface. This restores a more planar flame configuration seen in Fig. 4a decreasing S_T and, thus, setting up the next pulsation cycle.

It was observed in P15 that the magnitude of this instability depends non-monotonically on turbulent intensity reaching maximum strength at some intermediate values of U_l/S_L. In particular, when $U_l \lesssim S_L$, flame self-propagation is important and it attenuates the exponential growth of the flame surface. In contrast, at high turbulent intensities $U_l \gg S_L$, the flame is extremely tightly packed. This leads to frequent flame collisions, which interrupt the periods of exponential flame-surface growth and thus prevent the development of large-amplitude pulsations.

The second finding reported in P15 was the fact that such flame pulsations can result in a periodic formation of strong pressure pulses and even shocks. In particular, formation of shocks was observed with $Ma > 1.3$ in the course of flame interaction with $Ma_T = 0.02$ upstream turbulence. This is illustrated in Fig. 2a for case S18, which shows the formation of overpressures as high as 40%.

Formation of such pressure pulses occurs when S_T becomes a significant fraction of, or exceeds, the speed of a Chapman-Jouguet deflagration, S_{CJ} (Williams, 1985). We showed in an earlier work (Poludnenko *et al.*, 2011) that S_{CJ} serves as a threshold, at which the amount of energy generated inside the flame volume on its sound-crossing time becomes comparable to the internal energy of the fluid. This, in turn, results in the build-up of pressure, which can ultimately produce a catastrophic runaway process ending in a spontaneous deflagration-to-detonation transition (DDT). In fact, the ratio $CJ = S_T/S_{CJ}$ is effectively a reactive-flow counterpart of the Mach number. It serves as a figure of merit characterizing the importance of compressibility effects in a reaction wave, i.e., a flame, rather than a hydrodynamic wave as in the case of Mach number.

It is important to emphasize that, as shown in P15 and as will be demonstrated below, the onset of the pulsating instability of S_T does not require the formation of large overpressures. In fact, the latter are the consequence, rather than the cause, of the former. In those cases where the flame does produce overpressures, they can result in a significant amplification of turbulence inside the flame brush. This process can, in turn, alter the overall flame dynamics.

The mechanism of turbulence amplification is analo-

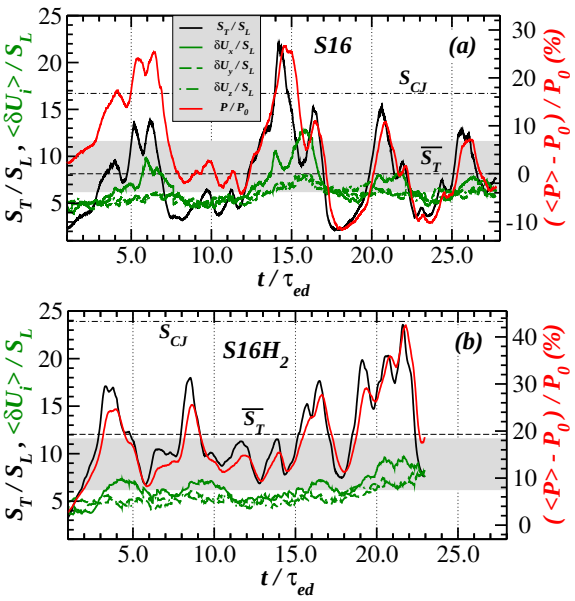

Figure 3. Comparison of the effect of a single-step and detailed H_2 kinetics on the pulsating instability. Shown are the key dynamical characteristics of the flame in simulations S16 (Poludnenko, 2015) and S16H_2 (see caption in Fig. 2 for the description). Note that the horizontal and left vertical axes in both panels have the same scale to facilitate comparison between the two cases.

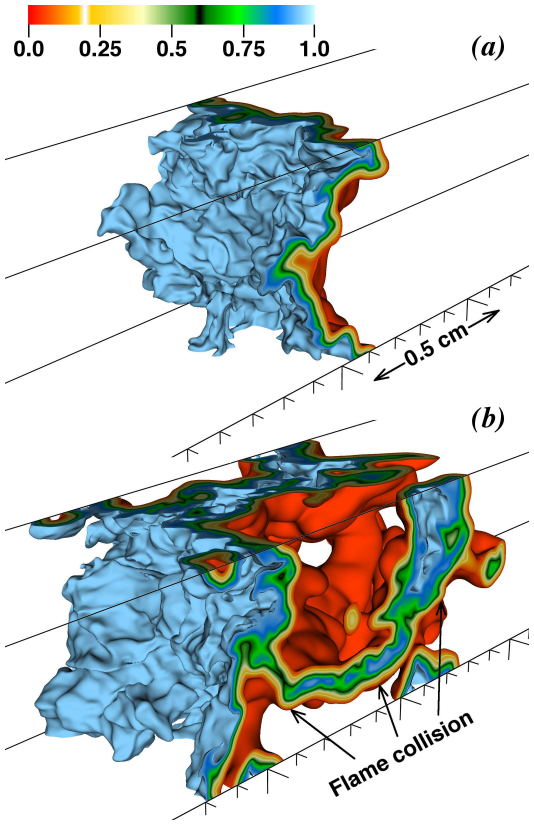

Figure 4. Change in the flame structure in the course of a typical flame pulsation in the calculation using single-step Arrhenius kinetics (case 16s described in Poludnenko (2015)). Shown is the flame volume bounded by the two isosurfaces of the fuel mass fraction $Y = 0.05$ (red) and $Y = 0.95$ (blue) at $t = 16.72\tau_{ed}$ (panel a) and $t = 19.13\tau_{ed}$ (panel b). These instances approximately correspond to the times of minimum and maximum flame burning velocity (reproduced from Poludnenko (2015)).

gous to that operating in a classical Richtmyer-Meshkov instability. Pressure gradients formed in the course of pulsations couple with density gradients across the flame front through the baroclinic term in the vorticity evolution equation, creating a powerful source of vorticity. Since both pressure and density gradients are preferentially aligned in the average direction of flame propagation, resulting turbulence amplification is strongly anisotropic, primarily affecting the streamwise velocity component. Such anisotropy of the velocity field inside the flame brush in case S18 is illustrated in Fig. 2a, which shows individual components of turbulent velocity fluctuations along each direction, $\langle \delta U_i \rangle$. Hereafter, $\langle ... \rangle$ indicates averaging over the flame-brush volume. It can be seen that the streamwise component, $\langle \delta U_x \rangle$, is significantly larger than the transverse components, $\langle \delta U_y \rangle$ and $\langle \delta U_z \rangle$, which mostly remain bounded by U_l and U_{rms} in the upstream flow (P15).

Such anisotropic turbulence amplification causes the flame to propagate with an average speed, which is much larger than the characteristic speed of upstream turbulent motions U_l. For instance in case S18 (Fig. 2a), S_T exceeds U_l by a factor of 3.62 on average and by a factor of 8.33 instantaneously. Note also that $\overline{S_T}$ is also larger than the upstream U_{rms} by almost a factor of 2.

The magnitude of turbulence amplification depends sensitively on the delicate interplay between the vortex stretching and baroclinic terms in the vorticity transport equation (P15). As a result, it also depends non-monotonically on the upstream turbulent intensity, similarly to the pulsating instability of the flame speed. At low U_l, turbulent flame speeds are not sufficiently high to create large overpressures required to produce significant baroclinic torque. On the other hand, with increase in U_l the strength of the regular vortex stretching term grows faster than that of the baroclinic term. As a result, even large overpressures in the presence of fast upstream turbulence contribute only modestly to the net vorticity production.

Analysis presented in P15 considered the effect of several factors on the flame stability, including turbulent intensity, system size, laminar flame speed (or Mach number), fluid density ratio across the flame, as well as temperature-dependent viscosity. Here we extend that work in two critical aspects.

First, all calculations described in P15 used a simplified single-step Arrhenius kinetics with temperature-dependent transport properties with unity Lewis number *Le*. While that single-step model is calibrated to reproduce all key properties of laminar flames and detonations in stoichiometric H_2-air mixtures, it is still an idealization. Thus, here we describe two DNS calculations, which demonstrate existence of the pulsating flame instability in two realistic, and dramatically different, systems: chemical flames in atmospheric H_2-air mixtures and thermonuclear flames in degenerate, relativistic plasmas found in stellar interiors.

The second issue that we investigate here concerns the dependence of the pulsating instability on the system size. In particular, results described in P15 showed that peak val-

Table 1. Summary of calculations performed

	Grid	$\frac{t_S}{\tau_{ed}}$	Da	CJ_L	$\frac{l}{\delta_L}$	$\frac{U_l}{S_L}$	$\frac{\overline{S_T}}{S_L}$	$\frac{S_T^{max}}{S_T^{min}}$	$\frac{P^{max}}{P^{min}}$	$\frac{\overline{\tau_P}}{\tau_{ed}}$	$\frac{\overline{\langle \delta U_x \rangle}}{S_L}$	$\frac{\overline{\langle \delta U_{y,z} \rangle}}{S_L}$
S16	$256^2 \times 8,192$	26.76	0.60	0.06	3.73	6.23	7.89	10.42	1.43	3.33	6.70	5.85
S16H$_2$	$256^2 \times 8,192$	21.89	0.60	0.04	3.71	6.22	12.05	7.19	1.39	2.78	6.37	5.41
S18	$512^2 \times 16,384$	10.05	5.94	0.06	14.92	2.49	9.01	4.34	1.31	0.91	8.52	3.80
S19v	$1,024^2 \times 32,768$	2.55	4.67	0.06	29.35	3.14	11.78	2.78	1.26	1.03	10.90	4.44
S20t	$512^2 \times 8,192$	10.41	7.20	0.008	19.69	2.74	4.53	2.71	1.01	2.07	2.04	2.12

See text for the definitions of various quantities. Note that for calculations S16 and S18, time-averaged values given here correspond to a somewhat larger time interval than in Poludnenko (2015). In particular, the averaging time interval here starts at $1\tau_{ed}$, while in Poludnenko (2015) it started at $5.5\tau_{ed}$.

ues of both S_T and $\langle P \rangle$ significantly increase with the system size (though, the amplitude S_T^{max}/S_T^{min} decreased). It is hard to settle this issue definitively due to the rapidly growing computational cost of DNS calculations associated with increasing domain sizes. Nevertheless, we take the next step in elucidating this question by performing arguably the largest DNS calculation to-date of a premixed turbulent flame with 32 billion zones. Key results from these three DNS are summarized below.

1 MODEL AND METHOD

Turbulence-flame interactions are modeled using compressible reactive-flow equations solved using a fully unsplit corner transport upwind scheme with the PPM spatial reconstruction and the HLLC Riemann solver (Gardiner & Stone, 2008) implemented in the code `Athena-RFX` (Stone *et al.*, 2008; Poludnenko & Oran, 2010). Turbulence is driven using a spectral method, which introduces in the flow divergence-free velocity fluctuations with a prescribed energy injection spectrum and rate (Poludnenko & Oran, 2010). This approach ensures that the turbulent integral velocity, U_l, and scale, l, in the upstream flow are nearly constant both in space and time with a standard deviation of $\lesssim 2\%$ and $\lesssim 5\%$, respectively. Detailed analysis of the resulting turbulence, both reacting and non-reacting, including comparison with prior experimental and DNS results, was presented in Hamlington *et al.* (2011, 2012).

Here we consider three reaction kinetics models. The first model is the one used in our previous studies (Gamezo *et al.*, 2008; Poludnenko, 2015). It uses a single-step, first-order Arrhenius kinetics. Equation of state is that of an ideal gas. A simplified reaction-diffusion model represents stoichiometric H_2-air mixture under $Le = 1$ conditions with model parameters calibrated to reproduce correct laminar flame and detonation properties.

Next we consider a detailed multi-step reaction model for hydrogen combustion based on the 2014 San Diego mechanism (Sánchez & Williams, 2014). This mechanism includes 21 reactions involving 8 reacting species H, H_2, O, O_2, OH, H_2O, HO_2, H_2O_2, and the inert N_2. Thermodynamic functions of pure chemical species are computed from the NASA seven-coefficient format (McBride *et al.*, 1993). Pure species shear viscosity coefficients and binary diffusion coefficients are evaluated from the standard kinetic theory expressions (Hirschfelder *et al.*, 1954). Thermal conduction coefficients of pure species are evaluated using expressions given by Warnatz (1982). Mixture-averaged conduction and shear viscosity coefficients are computed from averaging formulas of order 1/4 and order 6, respectively, as recommended by Ern & Giovangigli (1994). Mixture-averaged diffusion coefficients for each species are computed as in the TRANSPORT library (Kee *et al.*, 1986). In the interest of run-time performance, specialized source code for the chemical reaction source terms is generated from a CHEMKIN (Kee *et al.*, 1996) input file in a preprocessing step and subsequently compiled into Athena-RFX. The preprocessor generates code that evaluates the rates of change of species mass fractions and temperature due to chemical reactions and their analytical Jacobian generally following the formulation of Perini *et al.* (2012). Also generated by the preprocessor is a function that tabulates forward and reverse reaction rate constants and their temperature derivatives at start-up, so that they can be evaluated by interpolation. At run time, Athena-RFX reads CHEMKIN and TRANSPORT input files to obtain thermodynamic and transport property data. Polynomials for the mass-specific internal energy and constant-volume heat capacity are directly evaluated to initialize the solution and to solve for temperature given the conservative solution. Pure species transport properties are tabulated at start-up and subsequently evaluated by interpolation within Athena-RFX.

Finally, the third kinetics model that we consider represents thermonuclear burning in relativistic, degenerate plasmas, which are representative of conditions in stellar interiors during supernovae explosions (Hillebrandt & Niemeyer, 2000). In particular, Athena-RFX implements an α-chain network (Khokhlov *et al.*, 1997), which includes the triple-α, α-capture, and heavy-ion reactions for the following 13 isotopes: ^{4}He, ^{12}C, ^{16}O, ^{20}Ne, ^{24}Mg, ^{28}Si, ^{32}S, ^{36}Ar, ^{40}Ca, ^{44}Ti, ^{48}Cr, ^{52}Fe, and ^{56}Ni. Nuclear reaction rates are based on the tabulation by Caughlan & Fowler (1988) with screening corrections. Equation of state includes contributions from ideal ions, degenerate electrons, radiation, and electron-positron pairs (Timmes & Swesty, 2000). Thermal conduction includes both electron and photon components with the appropriate treatment of the degeneracy effects (Timmes, 2000). In the interest of computational efficiency, both the equation of state and thermal conduction are tabulated and use bi-quadratic run-time interpolation. Since in thermonuclear flames $Le \to \infty$ and $Pr \to 0$, diffusion and viscosity were not included in the physical model.

Treatment of general equations of state in Athena-RFX is implemented using the energy relaxation method of Coquel & Perthame (1998). The stiff system of equations both for chemical and thermonuclear kinetics is integrated using a non-iterative, single step, semi-implicit ODE integra-

tor YASS (Khokhlov *et al.*, 2012). It does not employ any approximations to the Jacobian matrix, conserves species mass fractions and total energy explicitly, and provides an excellent balance between accuracy and efficiency, which is critical for large-scale DNS.

All calculations are performed in a rectangular domain with a uniform Cartesian grid. Calculations S16, S18, and S19v use single-step kinetics, while calculation S16H$_2$ uses detailed H$_2$ kinetics (Fig. 1). Note that in contrast to cases S16 and S18, both cases S16H$_2$ and S19v include temperature-dependent viscosity. Case S20t uses thermonuclear kinetics. The flow is initialized with a uniform temperature T_0 and pressure P_0. In particular, in cases S16, S19, and S19v $T_0 = 293$ K, and in case S16H$_2$ $T_0 = 300$ K. In all of these calculations, $P_0 = 1.01 \times 10^6$ erg/cm^3 and initial mixture properties correspond to stoichiometric H$_2$-air. In the thermonuclear case, $T_0 = 10^8$ K and $P_0 = 2.2 \times 10^{25}$ erg/cm^3, and the fuel density is 10^8 g/cm^3. The initial mixture is pure ^{12}C.

Kinetic energy is injected at the scale of the domain width, L, with a constant rate for the duration of a simulation. Resulting turbulent flow in the upstream cold fuel is homogeneous and isotropic with an equilibrium Kolmogorov energy spectrum $\propto k^{-5/3}$ in the inertial range extending to scales $\lesssim \delta_L$. Boundary conditions are periodic in the y and z directions and zero-order extrapolations in the direction of flame propagation. The absence of unphysical effects due to the boundary conditions in our numerical approach, in particular, pressure wave reflections from the upstream/downstream boundaries, is demonstrated in P15.

In calculations S16 and S16H$_2$, grid resolution is $\Delta x = \delta_L/16$, while in cases S18 and S19v, $\Delta x = \delta_L/8$. With this resolution choice, in S16H$_2$ turbulence is somewhat under-resolved in the upstream cold flow with the Kolmogorov scale $\eta_f \approx 0.4\Delta x$ and is well resolved in product with $\eta_p \approx 4.4\Delta x$. In case S19v, turbulence is well resolved throughout the domain with $\eta_f \approx 2.2\Delta x$ and $\eta_p \approx 28\Delta x$. In the thermonuclear case S20t, $\Delta x = \delta_C/6$, where δ_C is the width of the ^{12}C-burning zone. Such resolution captures the speed of a laminar flame with an accuracy of a few percent.

In all cases, nonreacting turbulence was allowed to evolve in the domain over time periods between ≈ 2.5 and 5 eddy turnover times on the integral scale, τ_{ed}, before the flame was initialized. Subsequent one eddy turnover time after ignition was excluded from analysis to allow the flame to become fully developed. Table 1 shows the time interval t_S used for analysis in each case.

2 RESULTS AND DISCUSSION

Figure 2b shows development of the pulsating instability in case S19v. This calculation has twice larger domain size, and thus integral scale, than case S18 described in P15. Karlovitz number is the same in both cases ≈ 52 (see discussion of the definition of Ka in P15). An extremely large grid with 32 billion elements, which was used in case S19v, resulted in a significant computational cost of this DNS. In particular, this calculation required ≈ 22 million CPU hours on 65,536 cores on Garnet at the ERDC computing center. As a result, flow evolution in this case was followed over a shorter period of time compared to case S18.

Overall, both cases S18 and S19v show similar dynamics despite the fact that S19v has twice larger domain and also includes temperature-dependent viscosity with well resolved Kolmogorov scale throughout the domain. It can be seen that case S19v also develops pronounced pulsations. Peak burning velocities in both cases are comparable and they somewhat exceed S_{CJ}. This also results in comparable peak overpressures of $\approx 40\%$. Turbulence inside the flame brush in case S19v also undergoes strong anisotropic amplification with the time-averaged streamwise component $\overline{\langle \delta U_x \rangle}$ exceeding the average transverse components $\overline{\langle \delta U_{y,z} \rangle} \equiv \overline{\langle (\delta U_y + \delta U_z)/2 \rangle}$ by a factor 2.5 (Table 1). In both cases, transverse velocity components generally remain between U_l and U_{rms} in the upstream flow. Amplified turbulence inside the flame brush results in somewhat larger values of $\overline{S_T}$ in case S19v compared to S18, namely $11.78 S_L$ vs $9.01 S_L$. This, however, may not be statistically significant resulting from a shorter time-averaging interval.

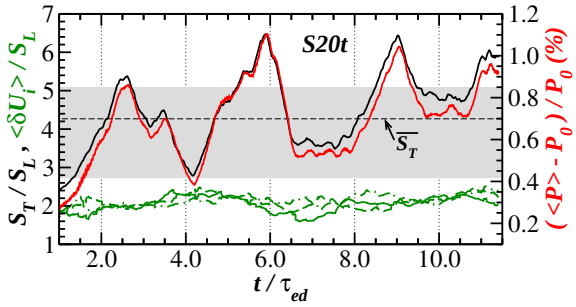

Figure 5. Pulsating instability in a turbulent thermonuclear flame. Shown is the evolution of the key dynamical characteristics of the flame in simulation S20t (see caption in Fig. 2 for description).

Several conclusions emerge from comparison of cases S18 and S19v. First, case S19v confirms that the presence of temperature-dependent viscosity with a fully resolved Kolmogorov scale does not have a pronounced effect on the instability. This observation was previously made in P15 based on a DNS with a 4 times smaller domain containing a somewhat under-resolved upstream turbulence. Second, doubling of the domain size compared to case S18 does not appear to increase the amplitude of either S_T or P. Note, however, that while Ka is the same in both calculations, Da is somewhat smaller in case S19v. This results in a stronger role played by flame self-propagation, which may attenuate the instability. We are currently performing a calculation similar to S19v, but which has the same Da as S18. This calculation along with S19v will show the relative impact of large-scale (or Da) vs. small-scale (or Ka) turbulence on the development of the pulsating instability. Results of this additional DNS will be presented in a separate paper.

Comparison of cases S16 and S16H$_2$ (Fig. 3) shows that flame pulsations are present even in the case of detailed multi-step chemistry with a realistic equation of state and transport processes. The overall amplitude of pulsations of S_T and P is somewhat smaller in S16H$_2$, while the time-averaged $\overline{S_T}$ is larger (also see Table 1). In particular, note that in S16, $\overline{S_T}$ is closer both to the upstream U_l (lower boundary of the shaded gray region) and turbulent velocity fluctuations inside the flame brush (green lines in Fig. 3a). In contrast, in case S16H$_2$, while $\langle \delta U_i \rangle$ are also close to U_l, $\overline{S_T}$ is larger and is practically equal to U_{rms} in the upstream flow. The cause of such higher burning velocity in the case of detailed chemistry requires further investigation.

Finally, Fig. 5 shows the evolution of S_T, $\langle P \rangle$, and $\langle \delta U_i \rangle$ in the case of a turbulent thermonuclear flame (case S20t). Turbulent conditions in this calculation, namely

l/δ_L, U_l/S_L, and Da are very similar to S18. While the pronounced pulsations of the burning velocity are present in S20t, their amplitude is smaller than in case S18 (Table 1). This agrees with the observation previously made in P15 that the strength of the instability diminishes with the density ratio across the flame, α. In particular, this effect was shown in P15 for an artificial single-step reaction-diffusion model with α decreased by a factor of 2 compared to case S18. Thermonuclear flames are characterized by values of $\alpha \lesssim 2$ due to the degeneracy of the electron gas (Timmes & Woosley, 1992). For instance, in case S20t, $\alpha = 1.87$. Thus, calculation S20t corroborates the dependence of the instability on α for a realistic reactive system. It is not clear, however, whether increase in the system size can partially offset the effect of α and increase the amplitude of pulsations. Note also that here, similar to case S16H$_2$, $\overline{S_T}$ is somewhat larger than both the upstream U_l and $\langle \delta U_i \rangle$, though S_T mostly remains between U_l and U_{rms} in the upstream flow. Finally, due to the extremely low value of $CJ_L = 0.008$, turbulent thermonuclear flame produced extremely weak pressure fluctuations on the order of $< 1\%$.

This work was supported by the Air Force Office of Scientific Research award F1ATA09114G005 and the National Aeronautics and Space Administration award NNH12AT33I. Computing resources were provided by the Department of Defense High Performance Computing Modernization Program under the Frontier project award, and by the Naval Research Laboratory.

REFERENCES

Bell, J. B., Day, M. S., Grcar, J. F. & Lijewski, M. J. 2006 Active control for statistically stationary turbulent premixed flame simulations. *Comm. App. Math. and Comp. Sci.* **1**, 29–51.

Candel, S *et al.* 2013 Advances in combustion and propulsion applications. *Eur. J. Mech. B - Fluid* **40**, 87–106.

Caughlan, G. R. & Fowler, W. A. 1988 Thermonuclear Reaction Rates V. *At. Data Nucl. Data Tables* **40**, 283.

Coquel, F & Perthame, B 1998 Relaxation of energy and approximate Riemann solvers for general pressure laws in fluid dynamics. *SIAM J. Num. Anal.* **35** (6), 2223–2249.

Ern, A & Giovangigli, V 1994 *Multicomponent Transport Algorithms*. Springer-Verlag, Heidelberg.

Gamezo, V. N, Ogawa, T & Oran, E. S 2008 Flame acceleration and DDT in channels with obstacles: Effect of obstacle spacing. *Combust. Flame* **155** (1–2), 302–315.

Gardiner, T.A & Stone, J.M 2008 An unsplit Godunov method for ideal MHD via constrained transport in three dimensions. *J. Comput. Phys.* **227**, 4123–4141.

Hamlington, P. E, Poludnenko, A. Y & Oran, E. S 2011 Interactions between turbulence and flames in premixed reacting flows. *Phys. Fluids* **23**, 125111.

Hamlington, P. E, Poludnenko, A. Y & Oran, E. S 2012 Intermittency in premixed turbulent reacting flows. *Phys. Fluids* **24**, 075111.

Hillebrandt, W. & Niemeyer, J.C. 2000 Type Ia supernova explosion models. *Annu. Rev. Astro. Astrophys.* **38**, 191–230.

Hirschfelder, C.F, Curtiss, C.F & Bird, R.B 1954 *Molecular Theory of Gases and Liquids*. John Wiley, New York.

Kadowaki, S & Hasegawa, T 2005 Numerical simulation of dynamics of premixed flames: Flame instability and vortex-flame interaction. *Prog. Energy Combust. Sci.* **31** (3), 193–241.

Kee, R.J, Dixon-Lewis, G, Warnatz, J, Coltrin, M.E & Miller, J.A 1986 A fortran computer code package for the evaluation of gas-phase multicomponent transport properties. *Sandia National Laboratories, Tech. Report* **SAND86-8245**.

Kee, R.J, Warnatz, J & Miller, J.A 1996 A fortran chemical kinetics package for the analysis of gas-phase chemical and plasma kinetics. *Sandia National Laboratories, Tech. Report* **SAND96-8216**.

Khokhlov, A, Domínguez, I, Bacon, C, Clifford, B, Baron, E, Hoeflich, P, Krisciunas, K, Suntzeff, N & Wang, L 2012 Three-dimensional simulations of thermonuclear detonation with α-network: Numerical method and preliminary results. *Advances in computational astrophysics: methods* **453**, 107–114.

Khokhlov, A. M., Oran, E. S. & Wheeler, J. C. 1997 Deflagration-to-Detonation Transition in Thermonuclear Supernovae. *Astrophys. J.* **478**, 678–688.

McBride, B.J, Gordon, S & Reno, M.A 1993 Coefficients for calculating thermodynamic and transport properties of individual species. *NASA Tech. Memo.* **4513**.

Nishiki, S, Hasegawa, T, Borghi, R & Himeno, R 2002 Modeling of flame-generated turbulence based on direct numerical simulation databases. *Proc. Combust. Inst.* **29**, 2017–2022.

Perini, Federico, Galligani, Emanuele & Reitz, Rolf D 2012 An analytical Jacobian approach to sparse reaction kinetics for computationally efficient combustion modeling with large reaction mechanisms. *Ener. Fuels* **26** (8), 4804–4822.

Poinsot, T & Veynante, D 2005 *Theoretical and Numerical Combustion*. R.T. Edwards, Inc.

Poludnenko, A. Y 2015 Pulsating instability and self-acceleration of fast turbulent flames. *Phys. Fluids* **27**, 014106.

Poludnenko, A. Y, Gardiner, T. A & Oran, E. S 2011 Spontaneous transition of turbulent flames to detonations in unconfined media. *Phys. Rev. Lett.* **107**, 054501.

Poludnenko, A. Y & Oran, E. S 2010 The interaction of high-speed turbulence with flames: Global properties and internal flame structure. *Combust. Flame* **157** (5), 995–1011.

Poludnenko, A. Y & Oran, E. S 2011 The interaction of high-speed turbulence with flames: Turbulent flame speed. *Combust. Flame* **158** (2), 301–326.

Sánchez, Antonio L & Williams, Forman A 2014 Recent advances in understanding of flammability characteristics of hydrogen. *Prog. Energy Combust. Sci.* **41** (C), 1–55.

Stone, J. M *et al.* 2008 Athena: A new code for astrophysical MHD. *Astrophys. J. Supp.* **178**, 137–177.

Timmes, F. X. 2000 Physical Properties of Laminar Helium Deflagrations. *Astrophys. J.* **528**, 913–945.

Timmes, F. X. & Swesty, F. D. 2000 The Accuracy, Consistency, and Speed of an Electron-Positron Equation of State Based on Table Interpolation of the Helmholtz Free Energy. *Astrophys. J. Supp.* **126**, 501–516.

Timmes, F. X. & Woosley, S. E. 1992 The conductive propagation of nuclear flames. I - Degenerate C + O and O + Ne + Mg white dwarfs. *Astrophys. J.* **396**, 649–667.

Warnatz, J 1982 Influence of transport models and boundary conditions on flame structure. In *Numerical Methods in Flame Propagation* (ed. N Peter & J Warnatz). Friedr. Vieweg and Sohn, Wiesbaden.

Williams, F. 1985 *Combustion Theory*. Perseus Books.